

**SOME FURTHER DEVELOPMENTS IN THE  
DYNAMIC MODELLING AND CONTROL OF THE  
LARGE ANGLE MAGNETIC SUSPENSION TEST FIXTURE**

Colin P. Britcher, Lucas E. Foster  
Department of Aerospace Engineering  
Old Dominion University  
Norfolk, VA

**SUMMARY**

A small-scale laboratory magnetic suspension system, the Large Angle Magnetic Suspension Test Fixture (LAMSTF) has been constructed at NASA Langley Research Center. This paper first presents some recent developments in the mathematical modelling of the system, particularly in the area of eddy current effects. It is shown that these effects are significant, but may be amenable to modelling and measurement. Next, a theoretical framework is presented, together with a comparison of computed and experimental data. Finally, some control aspects are discussed, together with illustration that the major design objective of LAMSTF - a controlled 360° rotation about the vertical axis, has been accomplished.

**INTRODUCTION**

In order to explore and develop technology required for the magnetic suspension of objects over large ranges of orientation, a small-scale laboratory development system, the Large Angle Magnetic Suspension Test Fixture (LAMSTF) has been constructed at NASA Langley Research Center. Possible applications for magnetic suspension systems of this general class include space payload pointing and manipulation, microgravity vibration isolation and wind tunnel model suspension [1]. An important objective of this particular project is to investigate the dynamic modelling of large-gap magnetic suspension systems, so that future systems can be designed with higher confidence levels.

**HARDWARE DESCRIPTION**

The general configuration [2] is illustrated in Figures 1,2. An array of five, room temperature, copper electromagnets are equally spaced on a 13.77 cm radius. The coils are wound with 509 turns of AWG 10 enamelled copper wire on bakelite forms, with mild steel cores. The electromagnets are mounted on an aluminum plate 1.27 cm thick. Each electromagnet is driven by a transistor switching power amplifier, rated at  $\pm 150$  V and  $\pm 30$  A continuous, with four-quadrant operation.

The suspended element consists of 16 wafers of Neodymium-Iron-Boron permanent magnet material, each 0.851 cm in diameter and 0.3175 cm thick, epoxied into an aluminum tube, 5.32 cm long and 0.9525 cm outside diameter. The total mass of the suspended element is 22.5 grams and the moment of inertia about tranverse axes

is  $5.5 \times 10^{-6} \text{ kg.m}^2$ . The direction of magnetization is along the axis of the cylinder, which is horizontal when suspended. The nominal magnetization is 954,930 A/m (1.2 Tesla), although measurements have indicated a slightly lower working value. The suspension height is 0.1m, measured from the axis of the suspended element to the top plane of the electromagnet conductor.

The position sensing system consists of multiple light beams, arranged in the vertical and horizontal planes, partially interrupted by the suspended element. The light sources are miniature infra-red light-emitting diodes, intended for use with fiber-optics, with collimating lenses added. The light receivers are matching infra-red phototransistors, with focussing lenses added. The complete sensor system is mounted on a framework which can be rotated by hand about a vertical axis. A schematic diagram of the sensor assembly is shown in Figure 3.

Several different control systems have been developed and demonstrated, including a simple analog version with phase-advance ("lead") compensation [2], a first-generation digital controller, generated using the bilinear (Tustin's) transformation [3,4], a decoupled PD controller [5], and LQR and LQG designs [4].

## EDDY CURRENT EFFECTS IN LAMSTF

### Introduction

Whenever a time-varying magnetic flux penetrates a conducting medium, eddy-currents will be generated. In the case of LAMSTF, the principal time variation is due to the necessary control forces and torques being generated by fluctuating electromagnet currents, since the system is open-loop unstable. In the original design, eddy-current circuits were deliberately introduced in three main areas, as illustrated in Figure 4 :

- 1) Position sensor structure,
- 2) Electromagnet cores,
- 3) Aluminum baseplate

This was done so that it would be necessary to measure, analyze and model the eddy current effects, rather than attempting to avoid their influence, as is the usual practice. The fact that stable suspension was initially achieved rather easily [2] was taken to indicate that the eddy current effects were not very significant. However, a consistent discrepancy has been found in the dynamic behaviour in the "pitch" degree-of-freedom, illustrated in Figure 5 [3,4]. In consequence, an analysis and modelling effort has now been undertaken.

### Eddy Current Modelling

A simplified analysis can be employed to assess the effects of eddy currents in LAMSTF. The two key assumptions are some a priori knowledge of the geometry of the eddy current circuit and that the circuit geometry be independent of frequency. The first assumption might require that the eddy currents be constrained to flow around well-defined paths, such as the position sensor structure here, rather than through large plates or shells of conducting material. Alternatively, the circuit geometry must be relatively simple and predictable. The second assumption requires that the "skin depth" be much greater than the local material thickness. The skin depth is given by the following formula [6] :

$$d = \sqrt{\left(\frac{2}{\mu_0 \mu_r \sigma \omega}\right)} \quad \text{or} \quad \sqrt{\left(\frac{2 \rho}{\mu_0 \mu_r \omega}\right)} \quad - (1)$$

- where  $d$  = Skin depth,  $\mu$  = Permeability,  $\rho = 1/\sigma$  = Resistivity,  $\omega$  = angular frequency. In the case of LAMSTF, the natural frequencies of the suspended element are rather low, of the order of 10Hz or less. For an aluminum conductor, the value at 10Hz would be around 28mm, much greater than the typical material thickness in LAMSTF. The only exceptions are the iron electromagnet cores, although it is found later that their influence is confined to higher frequencies.

If both of the above assumptions are satisfied, the resulting model corresponds to that commonly described in literature as the Single Time Constant Model. The derivation resembles the analysis of a transformer with a shorted secondary, as illustrated in Figure 6 :

$$V = IR + L \frac{dI}{dt} + L_{m_1} \frac{dI_{e_1}}{dt} + L_{m_2} \frac{dI_{e_2}}{dt} + \dots \quad - (2)$$

$$0 = I_{e_1} R_{e_1} + L_{e_1} \frac{dI_{e_1}}{dt} + L_{m_1} \frac{dI}{dt} \quad - (3)$$

- where  $R_{e_n}$ ,  $L_{e_n}$  are the resistance and inductance of the n'th eddy current circuit and  $L_{m_n}$  is the mutual inductance between the primary (the electromagnet coil) and the eddy current circuit. Note that mutual inductances between multiple eddy current circuits are neglected. The terminal characteristics of the primary (driven coil) can be found by combining these two equations :

$$\frac{I}{V} = \left( \frac{1}{(R + Ls) - \frac{(L_{m_1}s)^2}{R_{e_1} + L_{e_1}s} - \dots} \right) \quad - (4)$$

One special case is of interest here. Suppose that :

$$L = \alpha L_{e_1} \quad (0 \leq \alpha \leq \infty) \quad \text{and} \quad L_{m_1} = \beta \sqrt{L L_{e_1}} \quad (0 \leq \beta \leq 1) \quad - (5)$$

then :

$$\frac{I}{V} = \left( \frac{1}{(R + Ls) - \frac{\beta^2 \alpha (L_{e_1}s)^2}{R_{e_1} + L_{e_1}s} - \dots} \right) \quad - (6a)$$

but if  $R_{e_1} \rightarrow 0$  or  $s \rightarrow \infty$  :

$$\frac{I}{V} = \left( \frac{1}{R + Ls (1 - \beta^2)} \right) \quad - (6b)$$

This indicates that a non-dissipative (reactive) secondary effectively "turns off" part of the primary inductor. Continuing, the field components generated (at the suspended object) can be expressed as :

$$B_j = K_j I + K_{e_1} I_{e_1} + \dots = K_j I \left( 1 - \frac{K_{e_1} L_{m_1} s}{K_j (R_{e_1} + L_{e_1} s)} - \dots \right) \quad - (7)$$

where  $K_j$ ,  $K_{e_n}$  are constants representing the field generated at the suspension location by the electromagnet and the n'th eddy current respectively. Now the factor  $K_{e_n}$  will, in general, be different for each field component, that is each individual eddy current will

affect each field component by a different proportion. Therefore the eddy current effects in a system involving several electromagnets and eddy current circuits should be represented as follows :

$$[B_j] = [K_j] [I] + [K_{j_e}] [I_e] \quad - (8)$$

- where  $[B_j] = (B_x \ B_y \ B_z \ B_{xx} \ \dots)^T$ ,  $[I] = (I_1 \ I_2 \ \dots)^T$ ,  $[K_j]$  is a rectangular matrix of field coefficients and  $[K_{j_e}]$  is similar, though possibly of differing dimension. It is presumed that  $[I_e]$  can be derived from  $[I]$ , following equations 2,3.

Alternatively, if the eddy current circuit has similar geometry to the primary (for example the induced current in electromagnet cores), it can be argued that the relative effect on all field and field gradient components at the suspended object will be similar. In this case, the representation can be considerably simplified by invoking a false current as shown :

$$I' = \left( 1 - \frac{K_{e_1} L_{m_1} s}{K_j (R_{e_1} + L_{e_1} s)} + \dots \right) I, \quad \text{where } B_j = K_j I' \quad - (9)$$

It should be noted that the change in electromagnet terminal characteristics and the change in field at the model are two separate effects and should be modelled as such.

#### Determination of Parameters

The question now is, can the parameters  $K_{e_n}$ ,  $L_{e_n}$ ,  $R_{e_n}$  and  $L_{m_n}$  be estimated and/or measured with sufficient accuracy? First the problem of estimation is addressed.

Calculations have been carried out using the finite element computer code VF/GFUN, by Vector Fields Inc.. It should be noted that this code is magnetostatic and has no capability for direct eddy current calculations, although such codes are available (for instance ELEKTRA, by the same supplier). Instead, the code is used to calculate flux linkages, hence inductances, using :

$$\phi_{ij} = \sum_{j=1}^n L_{ij} I_j \quad - (10)$$

VF/GFUN calculates the field on a grid representing the linkage plane of the eddy current circuit. The field normal to the plane is then numerically integrated (by the OPERA pre- and post-processor) to yield the flux linkage term. Figure 7 illustrates the general arrangement. The calculation of the  $K_{e_n}$  terms is straightforward.

By way of example, a series of calculations has been made for a single LAMSTF electromagnet with a representation of one part of the position sensor assembly mounted on the same axis, as illustrated in Figure 8. The required parameters were predicted (or previously measured) to be :

$$\begin{aligned} L &= 0.0275 \text{ H} & R &= 0.74 \ \Omega \\ L_e &= 6.69 \times 10^{-7} \text{ H} & R_e &= 2.243 \times 10^{-4} \ \Omega \\ L_m &= 1.0998 \times 10^{-5} \text{ H} \end{aligned}$$

$$K_z = 3.495 \times 10^{-4} \text{ T} \quad K_{ze} = 4.369 \times 10^{-6} \text{ T}$$

Incorporating these values in equation 7, and examining the axial (z-axis) field component, gives :

$$B_z = K_z I \left( 1 - \frac{6.13 \times 10^{-4} \text{ s}}{1 + 2.983 \times 10^{-3} \text{ s}} \right) \quad - (11)$$

It is seen that the resonant frequency of this eddy current circuit is around 53Hz, significantly higher than LAMSTF open-loop natural frequencies, but still well within the range of interest.

### Experimental Verification

Actual measurements of the current to field transfer function, corresponding to equation 7, were made with an experimental set-up as described above, and later with LAMSTF. Field components were measured with a F.W. Bell Model 9903 Hall-effect gaussmeter. Electromagnet currents were measured using a current shunt. The transfer function was measured directly with a Schlumberger Model SI 1250 analyzer, with sine-sweep excitation. The results for an air-cored electromagnet with no eddy current circuits are shown in Figure 9, and are taken to represent the probe + instrument + data acquisition system response. These results are subtracted from all subsequent measurements. Figure 10 shows the measured transfer function for  $B_z$ , together with the predictions from equation 11. The agreement is thought to be satisfactory. The values of most parameters could be adjusted (refined) to give a better agreement, as shown in Figure 11. The only significant residual discrepancies are seen to occur at higher frequencies where the validity of the Single Time Constant Model is questionable.

The adjusted form of equation 11 is :

$$B_z = K_z I \left( 1 - \frac{7.591 \times 10^{-4} \text{ s}}{1 + 2.934 \times 10^{-3} \text{ s}} \right) \quad - (11b)$$

### More Complex Cases

If the electromagnet is mounted on the aluminum plate, a second eddy current circuit is added; when the iron core is inserted, a third is added. Figure 12 shows the comparison between experimental and computed responses. Again, the agreement is fair, although capable of improvement by refinement of parameter estimates, also shown in Figure 12. Note that, even if refinement of parameters is undertaken, the model does not correctly predict the high frequency behaviour, particularly where the iron core is present. This is due to the iron core becoming highly dissipative at these frequencies, due to its small skin depth.

An additional series of calculations and measurements has been made for the vertical field component generated at the centroid of the suspended element due to a LAMSTF electromagnet at the design location, i.e. with the sensor ring off-axis relative to the electromagnet. The geometry is illustrated in Figure 13 and typical computed and measured responses are shown in Figure 14. It is clear that the model is progressively less suitable for progressively more complex geometries.

Measurements have also been made with the full LAMSTF sensor frame in place. Examples are shown in Figure 15. Due to the geometrical complexity, with multiple interlocking eddy current paths, it has not yet been possible to compute reasonable estimates by the methods shown. It should be noted, however, that another assumption inherent in the form of the model previously chosen has been violated, that is the lack of interaction between separate eddy circuits. If these circuits are physically and electrically connected, this is clearly not reasonable.

### Terminal Characteristics

It appears to be possible to experimentally estimate certain important parameters without direct measurement of magnetic fields. Figure 16 shows a comparison of measured and computed terminal characteristics for the single LAMSTF electromagnet mentioned above. The agreement is not perfect, but sufficient to validate the approach and can, of course, be improved by adjustment of parameters.

## PART 2 - IMPLEMENTATION of LARGE ANGULAR ROTATION

### Linear Modelling

A portion of the development of the idealized governing equations for LAMSTF will be briefly reviewed here. Further details are given in References 7,8. The magnetic forces and moments acting on a magnetized core in a "large-gap" magnetic suspension system can be approximated as follows :

$$\vec{F}_c \simeq \nabla (\vec{M} \cdot \nabla B_o) \quad \vec{T}_c \simeq \nabla (\vec{M} \times \vec{B}_o) \quad (12)$$

- where  $\vec{M}$  represents the magnetization of the magnetic core in  $A/m$ ,  $\vec{B}$  the applied magnetic field in Tesla,  $\nabla$  is the volume of the magnetic core in  $m^3$ , and the subscript o indicates that the field or field gradient is evaluated at the centroid of the magnetic core. Now, following the detailed development presented in reference 9, the effect of changes in relative orientation between the magnetic core and the electromagnet array can be incorporated as follows :

$$\vec{F}_c = \nabla [T_m][\partial B][T_m]^{-1} \vec{M} \quad (13)$$

$$\vec{T}_c = \nabla \vec{M} \times ([T_m] \vec{B}) \quad (14)$$

Where a bar over a variable indicates magnetic core coordinates,  $[\partial B]$  is a matrix of field gradients and  $[T_m]$  is the coordinate transformation matrix from electromagnet coordinates to suspended element (magnetic core) coordinates. The axis systems and some nomenclature are clarified in Figure 17.

The fields and field gradients are created by an array of n electromagnets. Thus we can write :

$$\vec{B} = [K_B] \frac{\vec{I}}{I_{max}} \quad (15)$$

- where  $\vec{I} = (I_1, I_2, \dots, I_n)^T$  and  $[K_B]$  represents a matrix of field coefficients. Similarly, each element of  $[\partial B]$  can be written :

$$\partial B_{ij} = [ K_{\partial B_{ij}} ] \frac{\vec{I}}{I_{\max}} \quad (16)$$

At this stage, the equations are quite general, but will now be considerably simplified for the LAMSTF application. First, the magnetization of the suspended element is assumed to be along its principal ( $\bar{x}$ ) axis :

$$\vec{M} = ( M_{\bar{x}}, 0, 0 ) \quad (17)$$

Continuing, the only large rotation of the suspended element is assumed to take place about the z axis, so  $[T_m]$  becomes :

$$[T_m] = \begin{bmatrix} \cos \theta_z & \sin \theta_z & 0 \\ -\sin \theta_z & \cos \theta_z & 0 \\ 0 & 0 & 1 \end{bmatrix} \quad (18)$$

Substituting, expanding and collecting terms :

$$\begin{bmatrix} T_{\bar{y}} \\ T_{\bar{z}} \\ F_{\bar{x}} \\ F_{\bar{y}} \\ F_{\bar{z}} \end{bmatrix} = \begin{bmatrix} [KT] \\ [KF] \end{bmatrix} \vec{I} \quad (19)$$

- where :

$$[KT] = \begin{bmatrix} -[K_z] \\ -\sin \theta_z [K_x] + \cos \theta_z [K_y] \end{bmatrix} \quad (20)$$

$$[KF] = \begin{bmatrix} \cos^2 \theta_z [K_{xx}] + 2 \cos \theta_z \sin \theta_z [K_{xy}] + \sin^2 \theta_z [K_{yy}] \\ -\cos \theta_z \sin \theta_z [K_{xx}] + (\cos^2 \theta_z - \sin^2 \theta_z) [K_{xy}] + \cos \theta_z \sin \theta_z [K_{yy}] \\ \cos \theta_z [K_{xz}] + \sin \theta_z [K_{yz}] \end{bmatrix} \quad (21)$$

Now there are two related problems to solve. Firstly, the equilibrium currents required to support the weight of the suspended element may be found by using :

$$\begin{aligned} F_z = F_{\bar{z}} &= m_c g = \forall M_{\bar{x}} B_{\bar{x}\bar{z}} \\ T_{\bar{y}} = T_{\bar{z}} &= F_{\bar{x}} = F_{\bar{y}} = 0 \end{aligned} \quad (12)$$

- where  $m_c$  is the mass of the suspended element. Equation 19 can now be solved for

required currents as a function of yaw orientation  $\theta_z$ . As a point of interest :

$$B_{\bar{x}\bar{z}} = \frac{m_c g}{V M_{\bar{x}}} = 0.0962 \text{ Tesla/m in this case} \quad - (13)$$

Secondly, a decoupling matrix is required so that the controller can call for the appropriate combination of electromagnet currents to create the required forces and moments. This can be found by direct inversion of the [KT/KF] matrix from Equation 19, giving :

$$\vec{I}_{\text{demand}} = \begin{bmatrix} [\text{KT}] \\ [\text{KF}] \end{bmatrix}^{-1} \begin{bmatrix} T_{\bar{y}} \\ T_{\bar{z}} \\ F_{\bar{x}} \\ F_{\bar{y}} \\ F_{\bar{z}} \end{bmatrix}_{\text{demand}}$$

Note that the [KT/KF] matrix is a function of  $\theta_z$ . Initially, it has been found convenient to normalize the inverted [KT/KF] matrix column-by-column, with the normalization factor being incorporated into the loop gain.

The variable decoupling matrix is incorporated into the controller in the following way. Matrices are calculated at frequent intervals ( $6^\circ$  presently) and stored in memory. The controller interpolates in real-time between these matrices. The first three matrices, individually normalized, are shown here for reference :

$$\vec{I}_{\text{demand}\theta=0^\circ} = \begin{bmatrix} 0.7713 & 0 & 1 & 0 & -1 \\ 1 & 1 & -0.8091 & 0.6182 & -0.3092 \\ 0.8584 & 0.6178 & 0.3091 & -1 & 0.8092 \\ 0.8584 & -0.6178 & 0.3091 & 1 & 0.8092 \\ 1 & -1 & -0.8091 & -0.6182 & -0.3092 \end{bmatrix} \begin{bmatrix} T_{\bar{y}} \\ T_{\bar{z}} \\ F_{\bar{x}} \\ F_{\bar{y}} \\ F_{\bar{z}} \end{bmatrix}_{\text{demand}}$$

$$\vec{I}_{\text{demand}\theta=6^\circ} = \begin{bmatrix} 0.7637 & -0.1069 & 1 & -0.2091 & -1 \\ 0.9695 & 0.9340 & -0.6841 & 0.7474 & -0.409 \\ 0.8728 & 0.6841 & 0.1068 & -1 & 0.7472 \\ 0.8234 & -0.5112 & 0.5112 & 0.8708 & 0.8708 \\ 1 & -1 & -0.9339 & -0.4091 & -0.209 \end{bmatrix} \begin{bmatrix} T_{\bar{y}} \\ T_{\bar{z}} \\ F_{\bar{x}} \\ F_{\bar{y}} \\ F_{\bar{z}} \end{bmatrix}_{\text{demand}}$$

$$\vec{I}_{\text{demand}}_{\theta=12^\circ} = \begin{bmatrix} 0.7655 & -0.2091 & 0.9339 & -0.409 & -1 \\ 0.9405 & 0.8708 & -0.5111 & 0.8708 & -0.5112 \\ 0.8916 & 0.7472 & -0.1068 & -1 & 0.6841 \\ 0.7958 & -0.409 & 0.6840 & 0.7472 & 0.9339 \\ 1 & -1 & -1 & -0.209 & -0.1069 \end{bmatrix} \begin{bmatrix} T_{\bar{y}} \\ T_{\bar{z}} \\ F_{\bar{x}} \\ F_{\bar{y}} \\ F_{\bar{z}} \end{bmatrix}_{\text{demand}}$$

For this interpolation, the controller must have information as to the actual yaw orientation of the suspended element. It was realised that under certain circumstances this information could be deduced in near real-time from the observed behaviour of the suspended element, rather than by direct global measurement of the suspended element orientation, in at least two ways.

### A. Yaw Error Tracking

Suspension is established at a known reference orientation. If the sensor framework is now rotated (by hand) through some small angle, the suspended element will tend to become misaligned relative to the sensors. This yaw error signal is filtered to remove the effects of noise and the natural motion of the suspended element in response to small disturbances. Once the filtered error reaches a preset threshold, the controller steps through the array of decoupling matrices in an attempt to drive the yaw error back to zero. This method is rather crude, but has proven to be unexpectedly reliable.

### B. Current Distribution Analysis

The predicted current distributions required to suspend at various yaw orientations, together with actual measurements, are shown in Figure 18. It should be noted that the distributions are almost perfectly sinusoidal in nature. By straightforward analysis of an observed current distribution, again with some filtering to remove the effects of noise and so forth, it is possible to deduce the orientation of the suspended element.

In both cases, the algorithm cannot accommodate a steady-state applied yaw torque. Nevertheless, the fact that the position sensor framework does not require any form of angular orientation sensor is a great practical advantage. A sequence of photographs showing the system in operation is shown as Figure 19.

## DISCUSSION

The simple eddy current model proposed appears to be satisfactory in the case of large eddy current circuits in conducting, non-magnetic material. Relatively simple computations are capable of providing reasonable estimates of important parameters, with the option of refinement based on measurements of magnetic field or electromagnet terminal characteristics. In the case of the iron electromagnet cores, or at higher frequencies, more elaborate models have been proposed (for instance [9]), but these have one potentially serious drawback. This is that the greater the elaboration in the eddy current model, the more complex the overall suspension system model becomes, and the greater the potential difficulty in manipulating this model in the

process of controller synthesis using modern model-based design methods. In some applications, the simple model proposed, with parameter adjustment, may adequately describe the eddy current influence on the dynamic behaviour, hence control performance, of the system. Discrepancies at frequencies well outside (above) the controller bandwidth would be of no consequence.

## CONCLUSIONS

A simple model for the effect of eddy currents in the metallic structure of LAMSTF has been proposed and validated by experiment. However, it has not yet been possible to fully describe the eddy currents in the position sensor framework due to the geometric complexity involved.

Eddy currents have been shown to seriously affect field and field gradient components in the frequency range of interest, such that they must be incorporated into a system dynamic model if modern control synthesis techniques are to be fully successful.

The principal design objective of LAMSTF, the 360° rotation about the vertical axis, has been achieved.

## ACKNOWLEDGEMENTS

This work was supported by NASA Langley Research Center under Grant NAG-1-1056. The Technical Monitor was Nelson J. Groom of the Spacecraft Controls Branch. In addition, the authors wish to acknowledge the assistance of Thomas C. Britton of Lockheed Engineering and Sciences Company.

## REFERENCES

1. Britcher, C.P.: Large-Gap Magnetic Suspension Systems. International Symposium on Magnetic Suspension Technology. NASA Langley Research Center, August 1991. NASA CP-3152
2. Britcher, C.P.; Ghofrani, M.; Britton, T.; Groom, N.J.: The Large-Angle Magnetic Suspension Test Fixture. International Symposium on Magnetic Suspension Technology. NASA Langley Research Center, August 1991. NASA CP-3152
3. M. Ghofrani, Approaches to Control of the Large-Angle Magnetic Suspension Test Fixture. NASA CR-191890, December 1992.
4. Groom, N.J.; Britcher, C.P.: A Description of a Laboratory Model Magnetic Suspension Test Fixture with a Large Angular Capability. 1st IEEE Conference on Control Applications, Wright-Patterson AFB, September 1992.
5. Cox, D.; Groom, N.J.: A Decoupled Control Approach for a Large-Gap Magnetic Suspension System. 2nd International Symposium on Magnetic Suspension Technology, Seattle, WA, August 1993.
6. Stoll, R.L.: The Analysis of Eddy Currents. Clarendon, 1974
7. Groom, N.J.: Analytical Model of a Five Degree of Freedom Magnetic Suspension and Positioning System. NASA TM-100671, March 1989.
8. Groom, N.J.; Britcher, C.P.: Open-Loop Behaviour of Magnetic Suspension Systems Using Electromagnets Mounted in a Planar Array. NASA TP-3229
9. Buntenbach, R.W.: Improved Circuit Models for Inductors Wound on Dissipative Magnetic Cores. 2nd Asilomar Conference on Circuits and Systems, 1968.

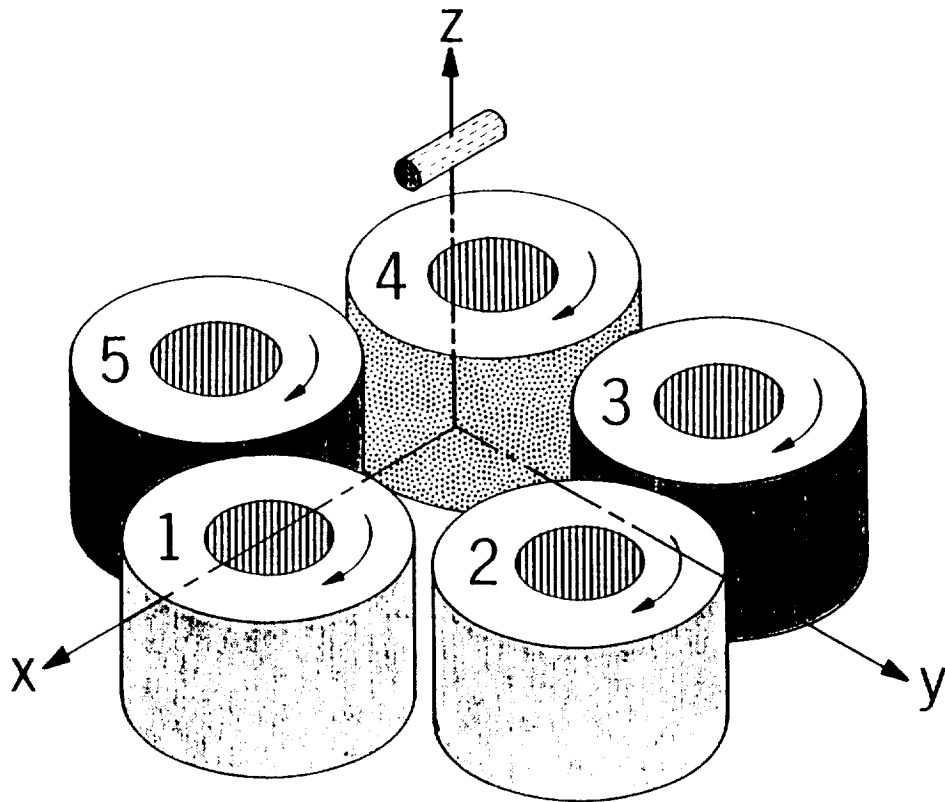


Figure 1 - General Arrangement of the Large Angle Magnetic Suspension Test Fixture

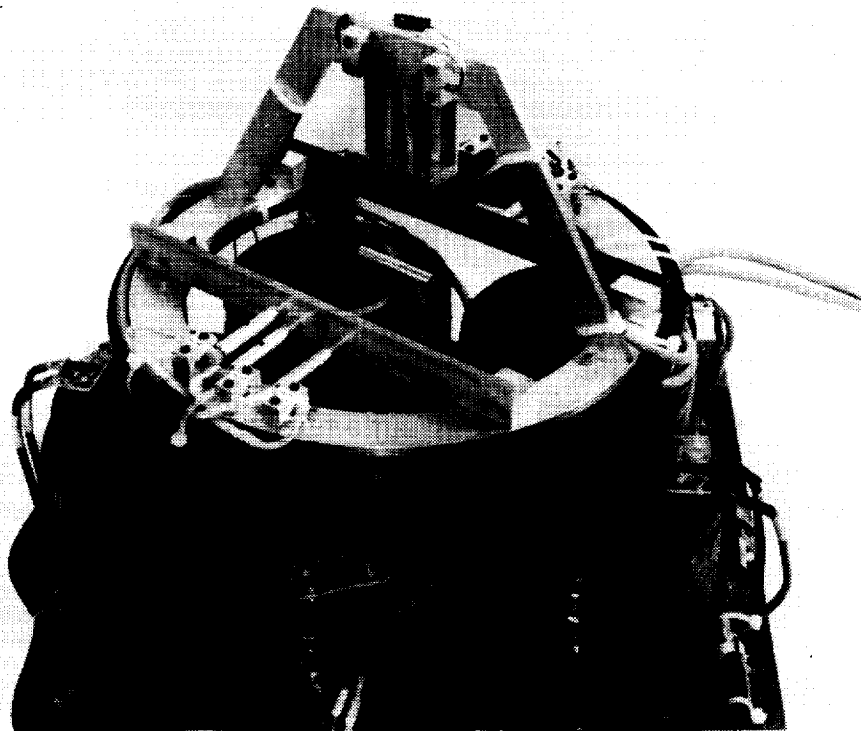


Figure 2 - The Large Angle Magnetic Suspension Test Fixture

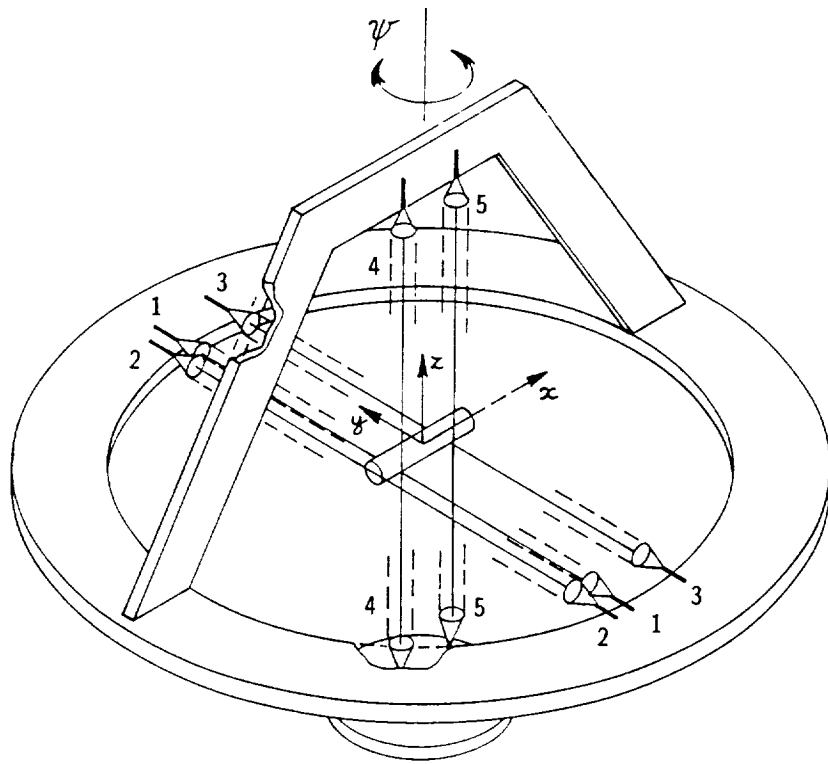


Figure 3 - Schematic Diagram of Optical System

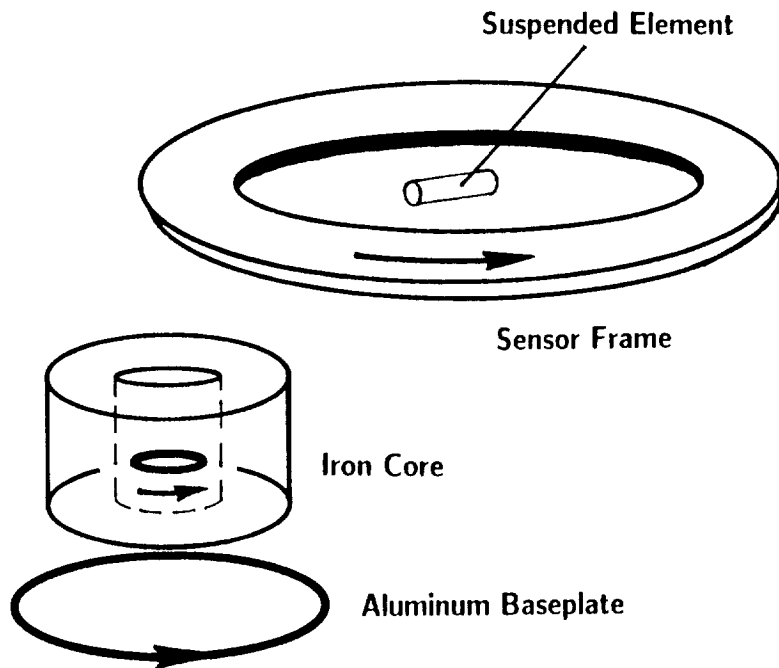


Figure 4 - Schematic Diagram of Eddy Current Circuits in LAMSTF

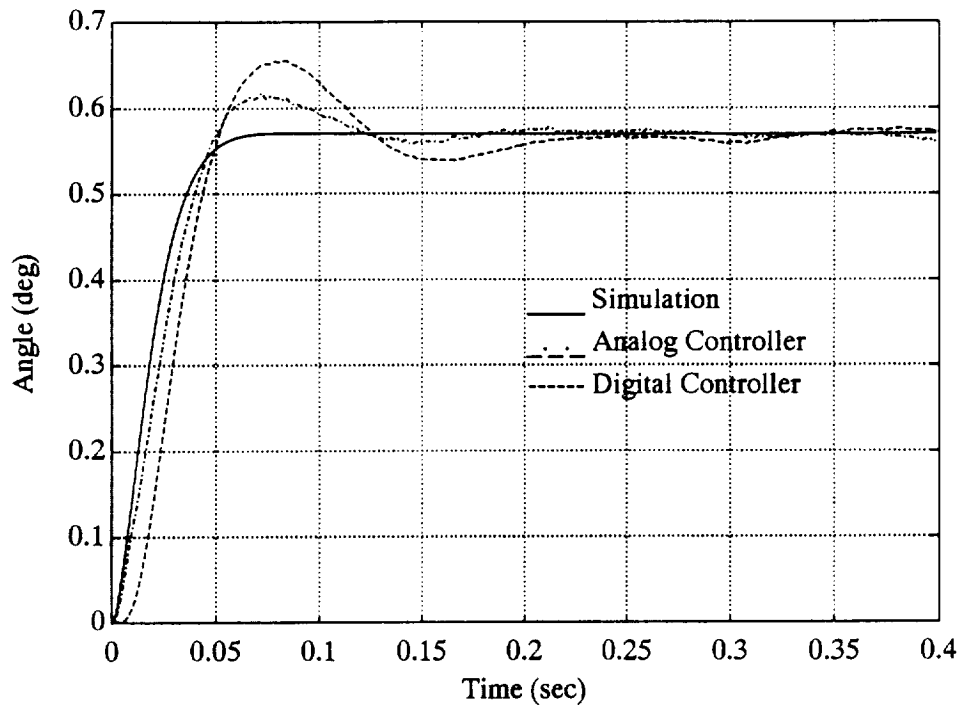


Figure 5 - Initial Discrepancy in Dynamic Response in Pitch ( $\theta_y$ )

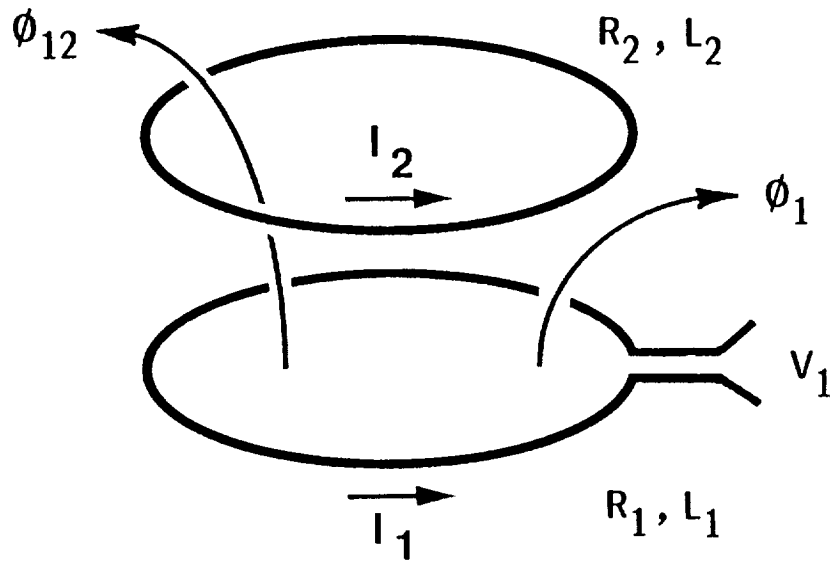


Figure 6 - Schematic of Circuit Model for Primary to Secondary Coupling

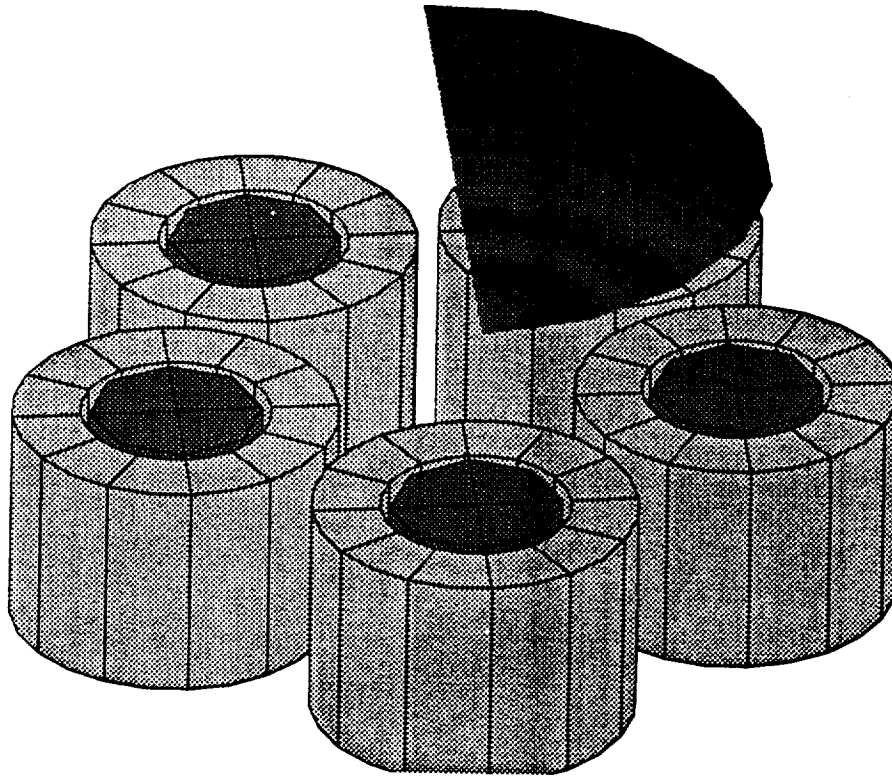


Figure 7 - Illustration of OPERA Flux Linkage Computation ( $B_z$  shown)

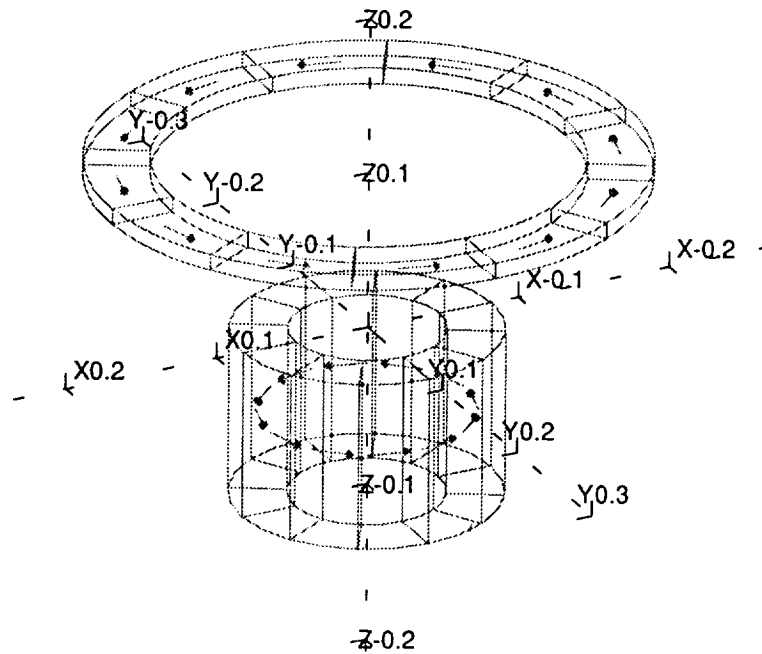


Figure 8 - Simplified Eddy Current Test Set-Up

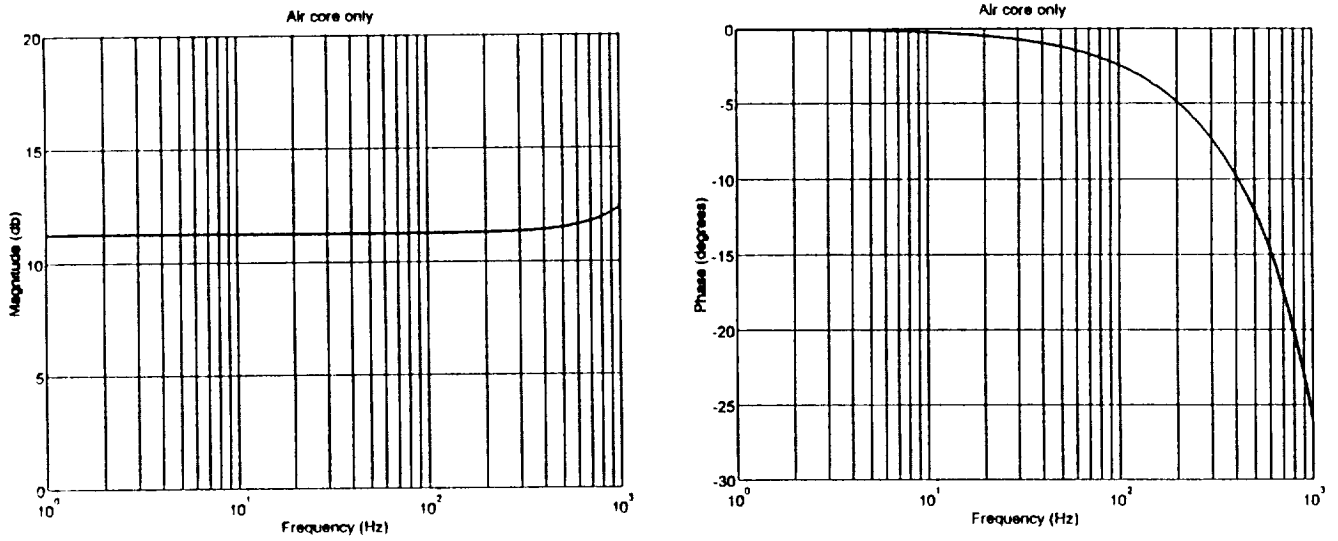


Figure 9 - Gaussmeter Probe Response

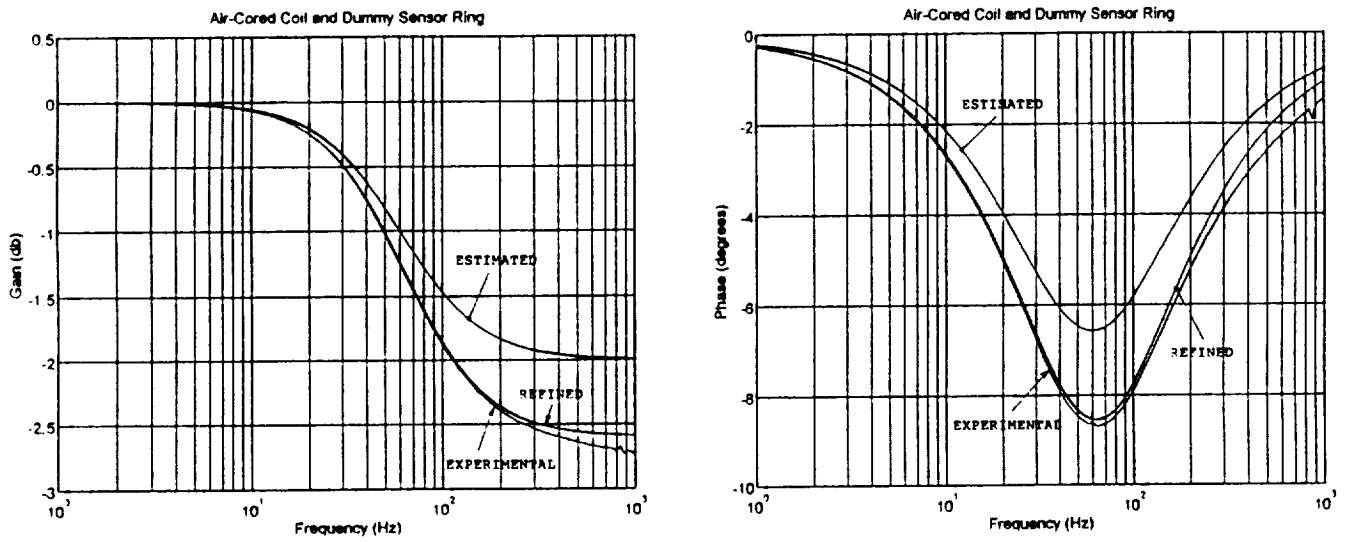


Figure 10 - Axial Field for Air-Cored Electromagnet and Dummy Sensor Ring

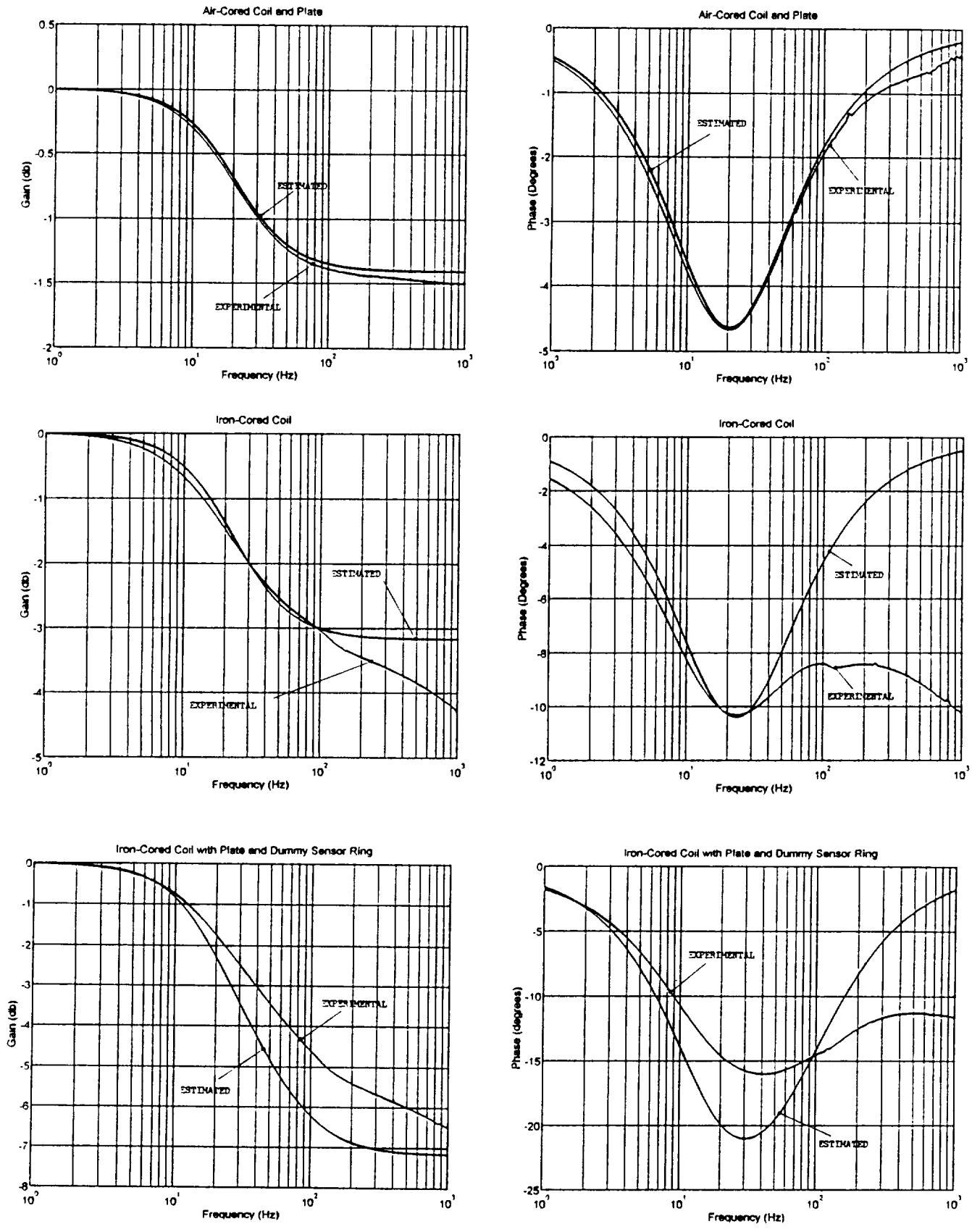


Figure 11 - Axial Field with Iron Core and Alloy Plate Added

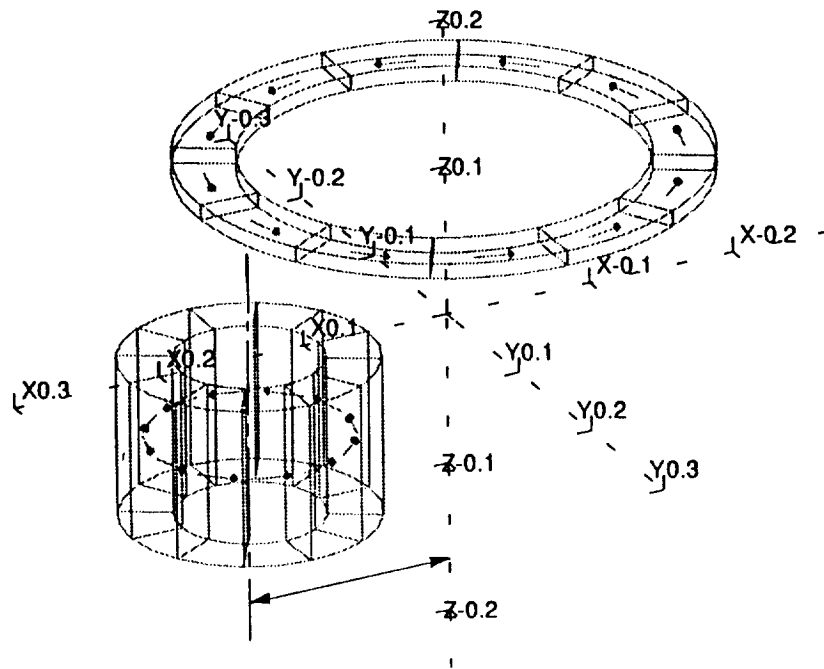


Figure 12 - Off-Axis Test Geometry

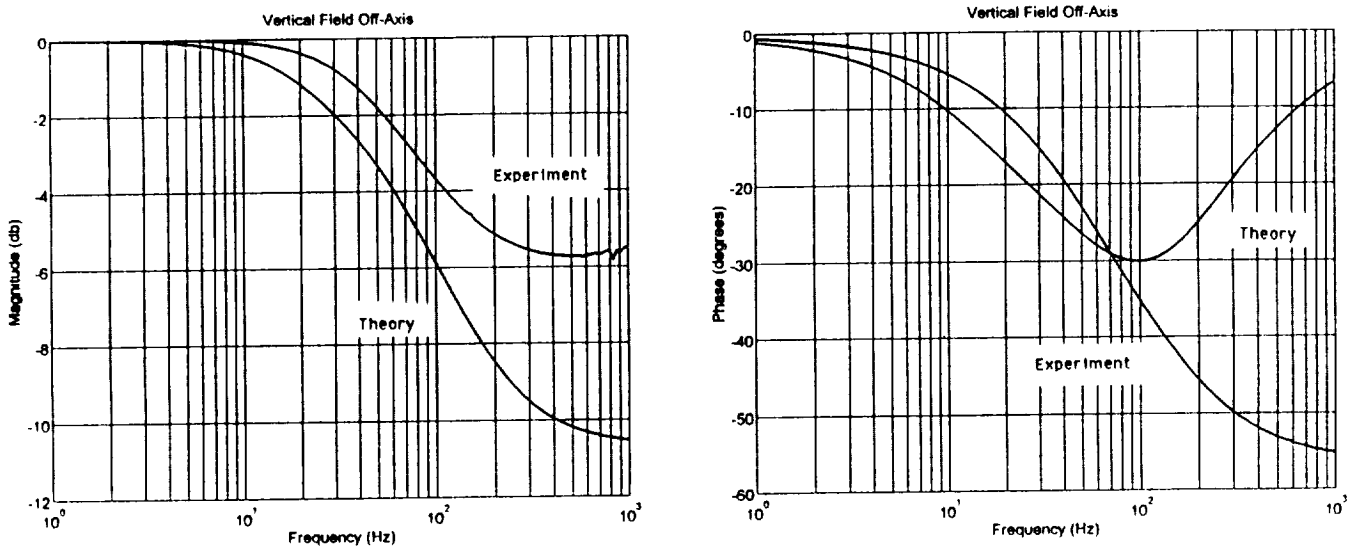


Figure 13 - Vertical Field with Off-Axis Test Set-Up

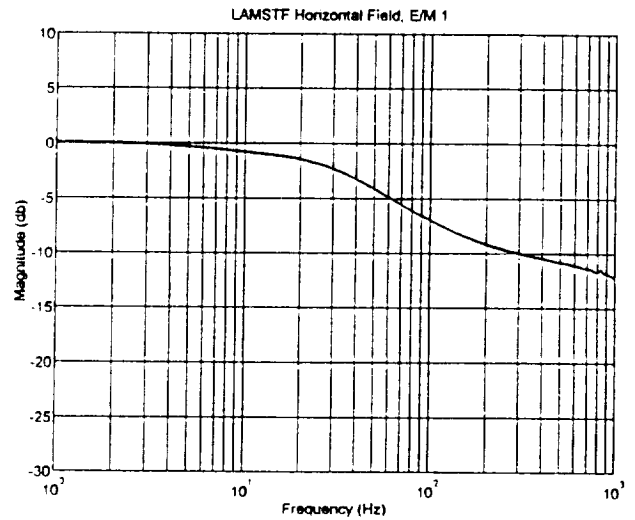
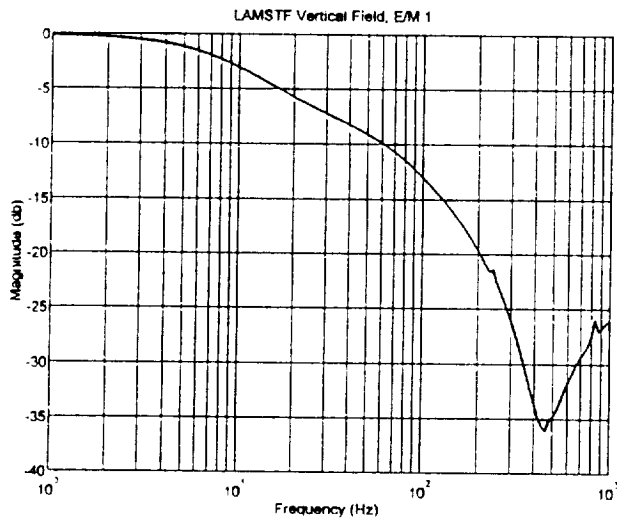


Figure 14 - Typical Field at Suspended Element with Full (Aluminum) Sensor Frame

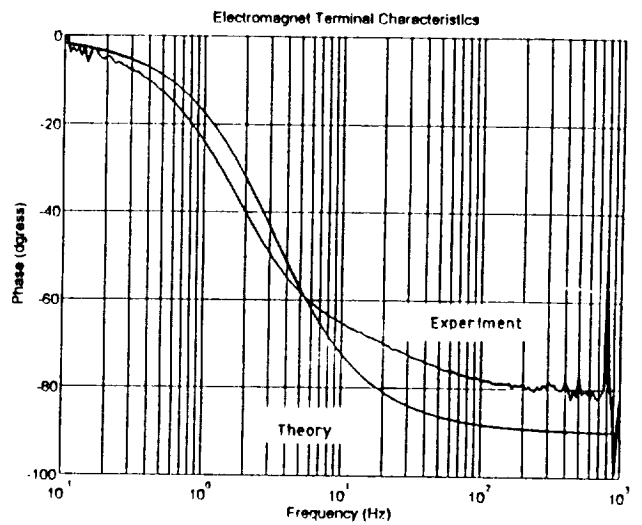
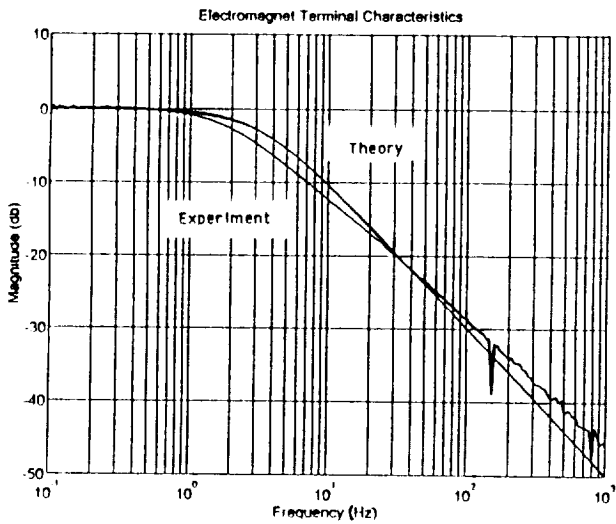


Figure 15 - Electromagnet Terminal Characteristics

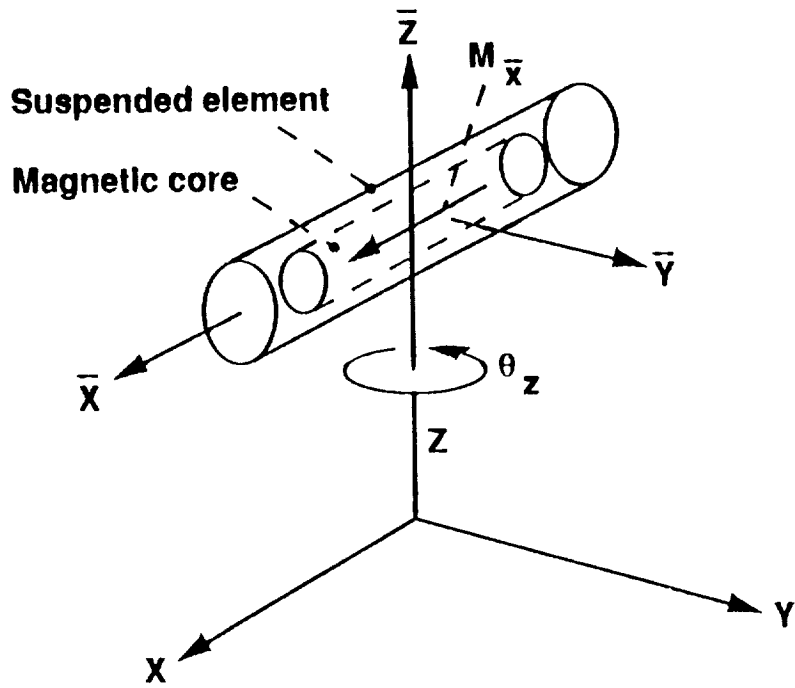


Figure 16 - Axis Systems and Nomenclature

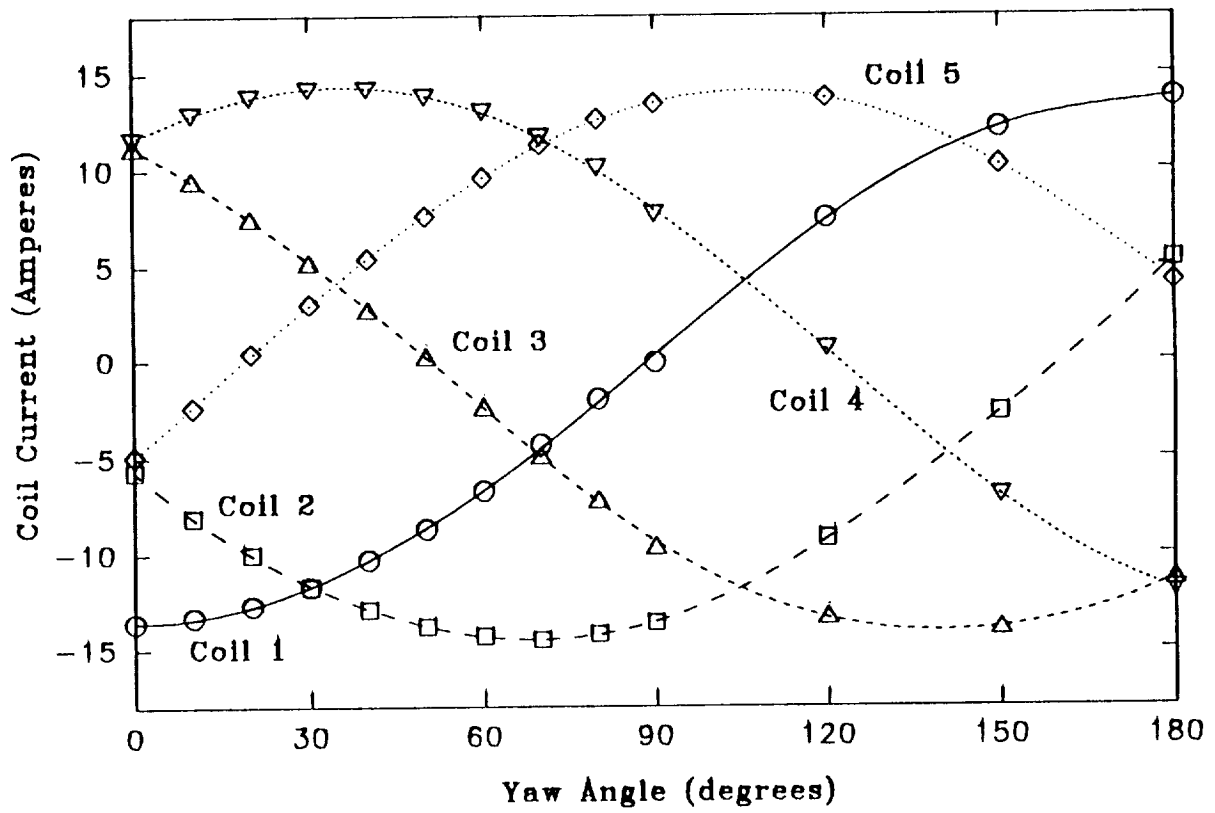
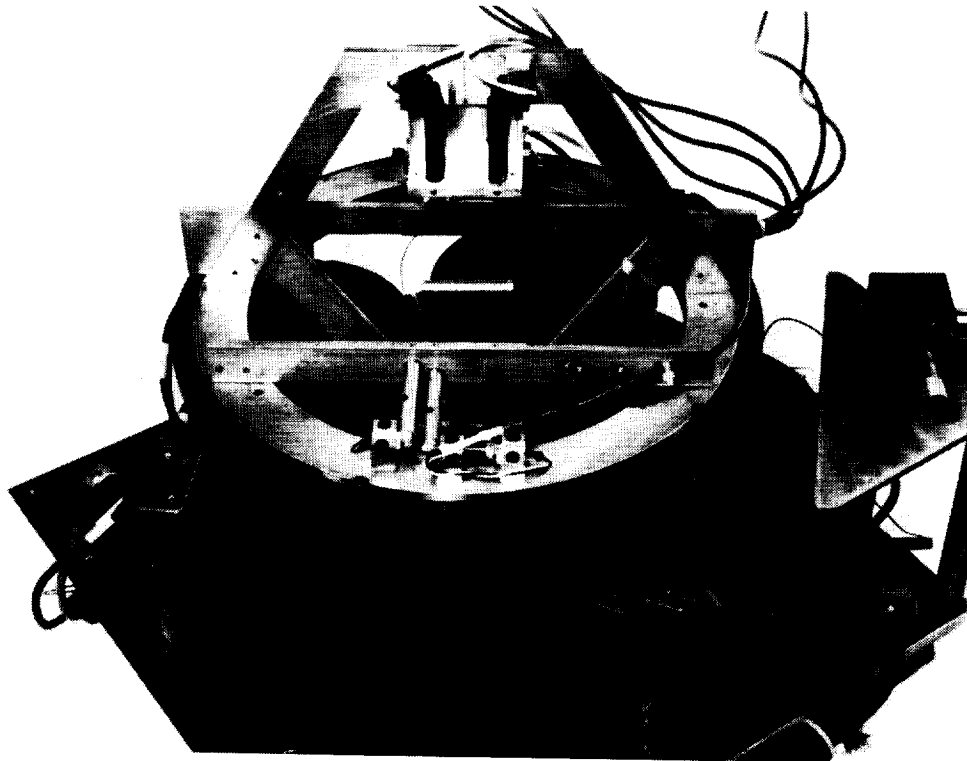


Figure 17 - Predicted Current Distributions for 180° Rotation



Practical Demonstration of Large Angular Rotation (0°)

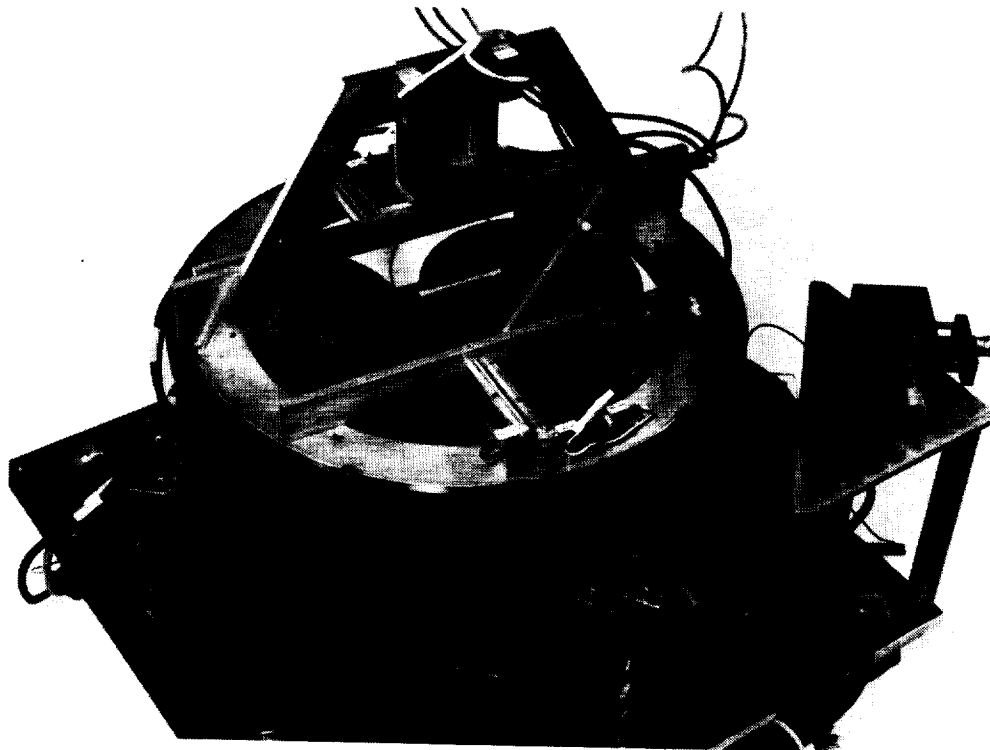
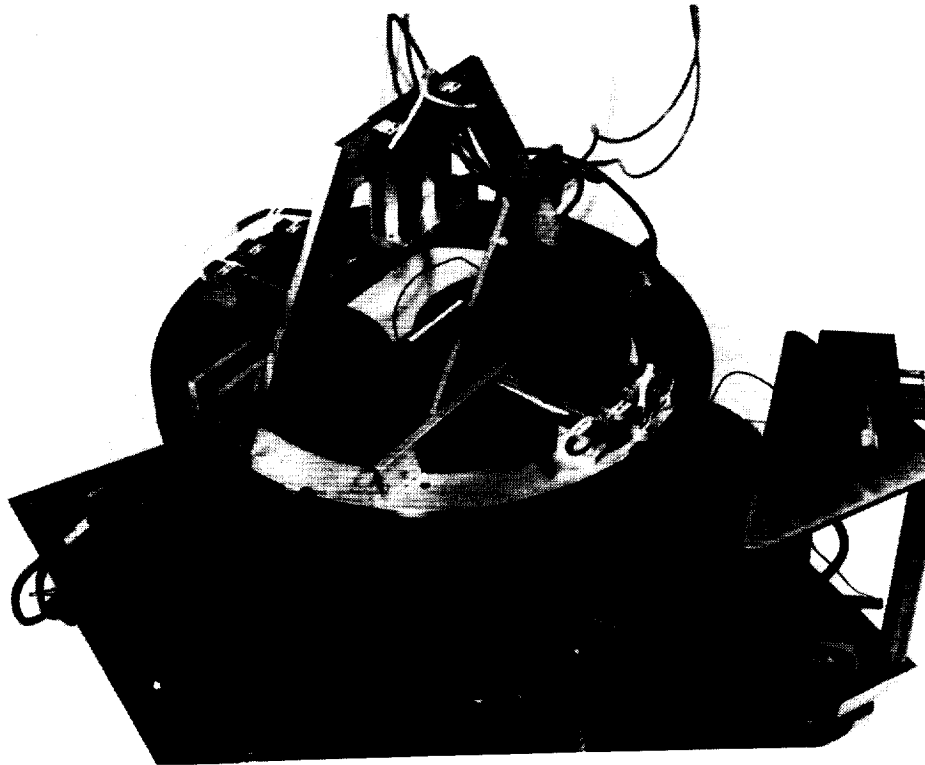


Figure 18 - Practical Demonstration of Large Angular Rotation (30°)



Practical Demonstration of Large Angular Rotation (60°)

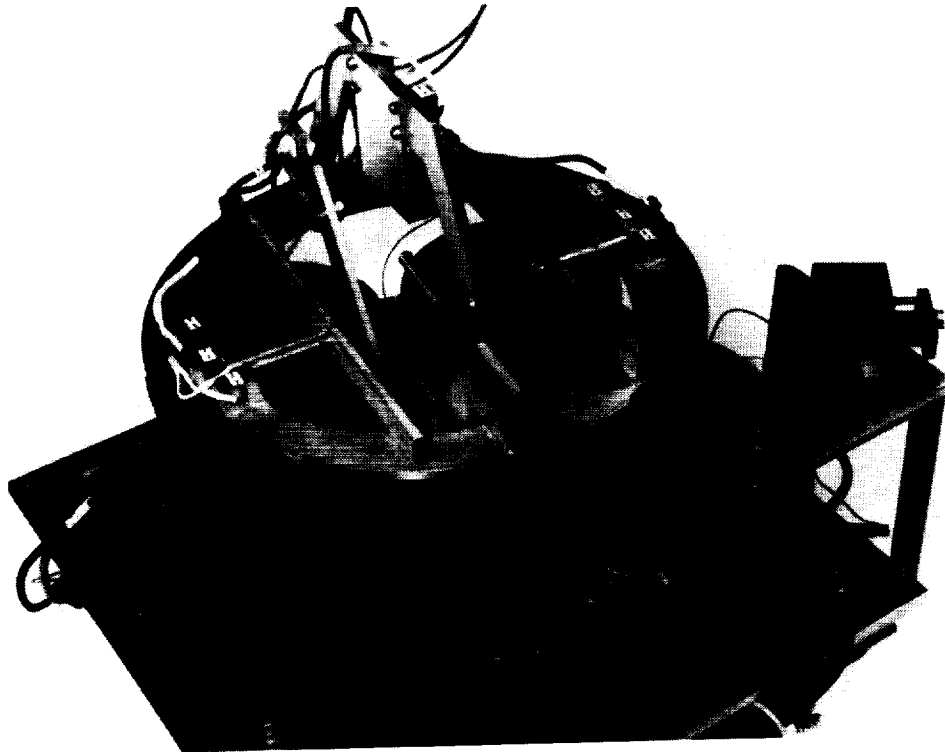


Figure 18 (concluded) - Practical Demonstration of Large Angular Rotation (120°)

OMH

## **Session 7b – Controls**

Chairman: Claude R. Keckler  
NASA Langley Research Center

